Systems/Circuits

Co-representation of Functional Brain Networks Is Shaped by Cortical Myeloarchitecture and Reveals Individual Behavioral Ability

Congying Chu,^{1,2} [©]Wen Li,^{1,3} Weiyang Shi,¹ Haiyan Wang,¹ Jiaojian Wang,⁴ [©]Yong Liu,⁵ Bing Liu,⁶ David Elmenhorst,^{2*} Simon B. Eickhoff,^{7,8*} Lingzhong Fan,^{1,3,9*} and [©]Tianzi Jiang^{1,3,9,10*}

¹Brainnetome Center, National Laboratory of Pattern Recognition, Institute of Automation, Chinese Academy of Sciences, Beijing 100190, China, ²Institute of Neuroscience and Medicine (INM-2), Forschungszentrum Jülich, Jülich 52428, Germany, ³University of Chinese Academy of Sciences, Beijing 100049, China, ⁴State Key Laboratory of Primate Biomedical Research, Institute of Primate Translational Medicine, Kunming University of Science and Technology, Kunming 650500, China, ⁵School of Artificial Intelligence, Beijing University of Posts and Telecommunications, Beijing 100876, China, ⁶State Key Laboratory of Cognitive Neuroscience and Learning, Beijing Normal University, Beijing 100875, China, ⁷Institute of Neuroscience and Medicine, Brain & Behaviour (INM-7), Forschungszentrum Jülich, Jülich 52428, Germany, ⁸Institute of Systems Neuroscience, Medical Faculty, Heinrich Heine University, Düsseldorf 40204, Germany, ⁹CAS Center for Excellence in Brain Science and Intelligence Technology, Institute of Automation, Chinese Academy of Sciences, Beijing 100049, China, and ¹⁰Xiaoxiang Institute for Brain Health and Yongzhou Central Hospital, Yongzhou 425000, Hunan Province, China

Large-scale functional networks are spatially distributed in the human brain. Despite recent progress in differentiating their functional roles, how the brain navigates the spatial coordination among them and the biological relevance of this coordination is still not fully understood. Capitalizing on canonical individualized networks derived from functional MRI data, we proposed a new concept, that is, co-representation of functional brain networks, to delineate the spatial coordination among them. To further quantify the co-representation pattern, we defined two indexes, that is, the co-representation specificity (CoRS) and intensity (CoRI), for separately measuring the extent of specific and average expression of functional networks at each brain location by using the data from both sexes. We found that the identified pattern of co-representation was anchored by cortical regions with three types of cytoarchitectural classes along a sensory–fugal axis, including, at the first end, primary (idiotypic) regions showing high CoRS, at the second end, heteromodal regions showing low CoRS and high CoRI, at the third end, paralimbic regions showing low CoRI. Importantly, we demonstrated the critical role of myeloarchitecture in sculpting the spatial distribution of co-representation by assessing the association with the myelin-related neuroanatomical and transcriptomic profiles. Furthermore, the significance of manifesting the co-representation was revealed in its prediction of individual behavioral ability. Our findings indicated that the spatial coordination among functional networks was built upon an anatomically configured blueprint to facilitate neural information processing, while advancing our understanding of the topographical organization of the brain by emphasizing the assembly of functional networks.

Key words: co-representation; functional brain network; myeloarchitecture; resting-state fMRI

Received May 10, 2023; revised Jan. 16, 2024; accepted Jan. 20, 2024.

Author contributions: C.C., S.B.E., L.F., and T.J. designed research; C.C., W.L., W.S., H.W., D.E., S.B.E., L.F., and T.J. performed research; C.C., J.W., Y.L., B.L., D.E., and T.J. contributed unpublished reagents/analytic tools; C.C., W.L., L.F., and T.J. analyzed data; C.C., S.B.E., L.F., and T.J. wrote the paper.

This work was supported by the following sources: STI2030-Major Projects (Grant No. 2021ZD0200200), the National Natural Science Foundation of China (Grant Nos. 62250058, 82151307, and 82072099), the Strategic Priority Research Program of Chinese Academy of Sciences (XDB32030200), Scientific Project of Zhejiang Lab (Grant No. 2022KI0AC02), and ANSO Joint Project (Grant No. ANSO-CR-KP-2022-10). Data were provided (in part) by the Human Connectome Project, WU-Minn Consortium (Principal Investigators: David Van Essen and Kamil Ugurbil; 1U54MH091657) funded by the 16 NIH Institutes and Centers that support the NIH Blueprint

for Neuroscience Research; and by the McDonnell Center for Systems Neuroscience at Washington University. We (C.C. and D.E.) thank the "2019 Helmholtz — OCPC — Program for the involvement of postdocs in bilateral collaboration projects" for their financial support that enabled this study. We thank Rhoda E. and Edmund F. Perozzi, PhDs, for their English language and editing assistance.

*D.E., S.B.E., L.F., and T.J. are the senior authors.

The authors declare no competing financial interests.

Correspondence should be addressed to Tianzi Jiang at jiangtz@nlpr.ia.ac.cn or Lingzhong Fan at lingzhong.fan@nlpr.ia.ac.cn.

https://doi.org/10.1523/JNEUROSCI.0856-23.2024

Copyright © 2024 the authors

Significance Statement

The human brain is functionally organized into large-scale functional networks that are highly structured in space and time. How these networks are coordinated by the physical embedding of the brain in space is still unclear. We propose the co-representation of functional networks, as a new concept accompanied by two quantitative indexes, to characterize the spatial coordination between networks. We found that the co-representation pattern was anchored along a sensory–fugal axis of cytoarchitectural classes. This pattern is shaped by the cortical myeloarchitecture, demonstrated by both neuroanatomical and transcriptomic data. The manifestation of co-representation is a reliable predictor of individual behavioral performance. Our findings indicate the co-representation of functional networks is built upon an anatomically configured blueprint to support neurocognitive computations.

Introduction

The human brain is functionally organized into a set of macroscale functional networks subserving complex behaviors (Mesulam, 1990; Power et al., 2011; Yeo et al., 2011). With the recent advances in network neuroscience (Bassett and Sporns, 2017), functional networks have gained traction to characterize the localized functions in brain areas and their neurocognitive relevance (Genon et al., 2018; Ito et al., 2020b), emerging as an important window into distributed information processing in the human brain. Understanding how the brain navigates the coordination among the functional networks that are highly structured in space and time remains an imperative neuroscientific endeavor that will provide fundamental insights into the information-processing architecture of the human brain.

Accumulating evidence from multiple independent efforts suggests that functional networks are coordinated to harness cognitive functionality. Specifically, the interaction between the brain functional networks has been demonstrated to efficiently predict a set of neurocognitive functions (Sui et al., 2020; Chen et al., 2022), such as attention (Rosenberg et al., 2016; Wu et al., 2020) and working memory (Yamashita et al., 2018), even with linear models. Also, the spatial topography of multiple functional networks has been found to collectively predict, for example, executive function (Cui et al., 2020) and reading ability (Kong et al., 2019). In contrast, disrupting the coordination between the functional networks can be biomarkers of major psychiatric and neurological disorders to predict clinical symptoms (Dadi et al., 2019; Cui et al., 2022). Consistent with the triple network model (Menon, 2011), the joint dysfunction of functional networks across psychiatric disorders reflects the complex coordination between them (Sha et al., 2019; Perovnik et al., 2022). More inherently, direct evidence has shown that the temporal correlations between brain functional networks are influenced by genetic factors, highlighting the potential genetic controls on the layout of brain functional networks (Yang et al., 2016; Zhao et al., 2022). Therefore, the coordination among functional networks is a fundamental facet of interest in the human brain's functional organization.

However, traditional measures of network coordination mainly focused on the relationship between functional networks, which cannot adequately capture the spatial configuration, such as the distinct roles of brain areas in reconciling the network-by-network coordination, about how the brain maintains it. Especially, compared with the previous studies that investigated the functional brain networks mainly based on predefined atlases (ROI-based; subjected to the selection of brain atlases), it is still not clear how we could pattern the spatial coordination of functional

networks in a continuous manner (vertex-wise; versatile in different scenarios). Without the quantified distribution of coordination, it would be largely hampered to further investigate the neural basis and the biological relevance for manifesting the coordination among functional networks. Therefore, based on the canonical individualized functional networks, we addressed the fundamental question about the spatial configuration of network coordination by bringing up the concept of co-representation that is defined at each brain location, that is, vertex-wise, as a one-dimensional vector composed of the extent to which the activity of each network expresses here.

To outline the spatial distribution pattern of co-representation for illustrating the distinct roles of brain areas in facilitating network coordination, we proposed two unitless vertex-wise indexes from complementary aspects, that is, the co-representation specificity index (CoRS) and the co-representation intensity index (CoRI). CoRS was expected to capture to what extent the co-representation was driven by specific networks by measuring the anisotropy among the expression values of networks at a brain location. CoRI was expected to reflect the overall expression of networks at a brain location. Furthermore, having known the evidence that the emergence of brain functions was under structural and genetic constraints (Burt et al., 2018; Suarez et al., 2020; Zachlod et al., 2022), it would be worth digging into the biological underpinnings of the captured pattern, which could contribute to a more complete understanding of the network coordination. Especially, given the important role of myelination in the information transfer in the human brain (Glasser et al., 2014; Salzer and Zalc, 2016), it was remarkable to evaluate the effect of the cortical myeloarchitecture. Meanwhile, discovering the neurocognitive relevance of the captured pattern might facilitate our understanding of the biological significance of having the coordination of brain functional networks. An overview of how these aspects were juxtaposed was shown in Figure 1.

Our analyses revealed that both CoRS and CoRI have spatially stable distribution across multiple hierarchical levels of network granularities and between datasets, situating the roles of brain regions in network coordination along a sensory–fugal cytoarchitectural axis. With the captured patterns, we can demonstrate the role of myeloarchitecture in sculpting the spatial pattern of co-representation by establishing links between the two indexes and the multifaceted cortical myelin content presented in neuroanatomical and gene expression profiles. We further assessed the biological relevance of manifesting network coordination by leveraging the two indexes to predict individual behaviors. These results present a new view on the spatial configuration embedded in the brain network

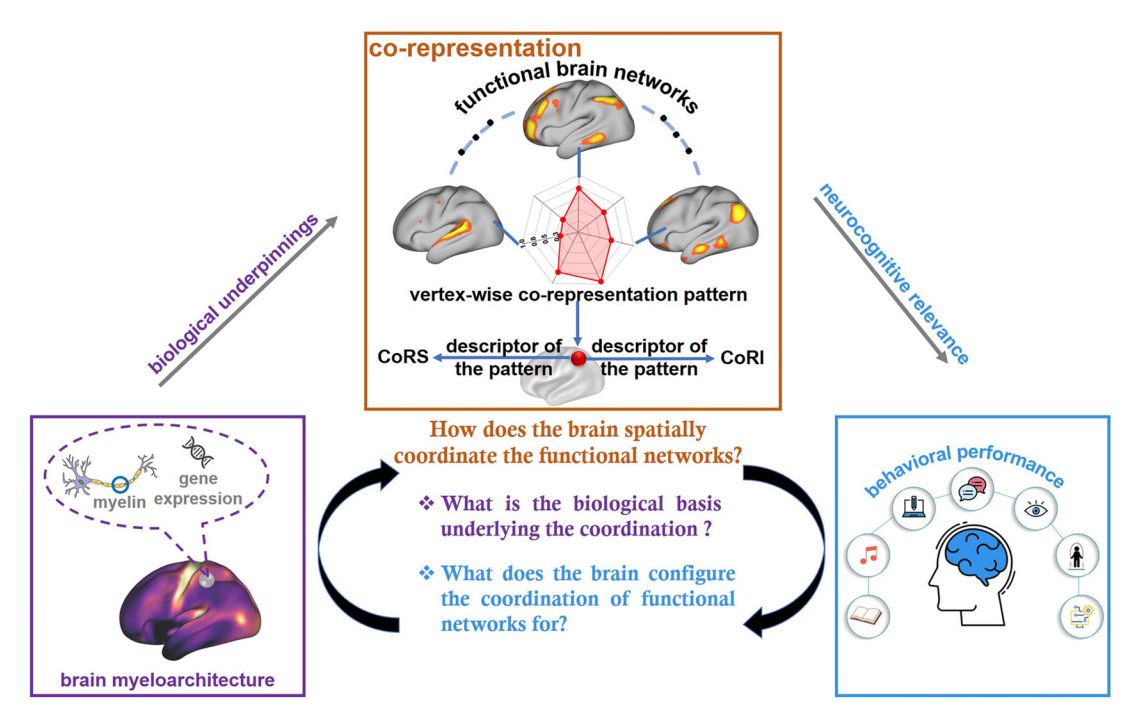


Figure 1. Overview of the current study on the co-representation of functional networks in the human brain.

coordination and highlight its neurobiological underpinnings and neurocognitive meanings.

Materials and Methods

We here introduced the analytic details for characterizing the co-representation of RSNs. Based on the spatial distributions of RSNs and their temporal activities derived by the decomposition of individual rfMRI data with the reference from the group independent component analysis (ICA), we defined two indexes, that is, CoRS and CoRI, to describe the topological signatures of co-representation for each cortical vertex in each individual. To illustrate the neurobiological underpinnings and the neurocognitive relevance of the captured pattern of co-representation, we further capitalized on multimodal neuroimaging, transcriptomic, and behavioral evidence. More details would be available in the following part.

MRI data and preprocessing. In this study, rfMRI data from the Human Connectome Project (HCP S1200 release) were used (Van Essen et al., 2013). Only healthy participants who had 4×15 min runs of rfMRI data were included (1,003 participants, ages 22-37 years, 534 females). The rfMRI data were acquired on a 3 T Siemens Connectome-Skyra scanner with gradients customized for the HCP. Briefly, a gradient-echo echo-planar imaging (EPI) sequence (1,200 time frames; TR = 720 ms; TE = 33.1 ms; flip angle, 52°; 2.0 mm isotropic voxels; multiband factor, 8) was adopted for scanning each run of rfMRI data, which was collected with the participants' eyes open. More details about the rfMRI acquisition are available in the published description of the HCP database (Ugurbil et al., 2013). For the rfMRI data preprocessing, we adopted the preprocessed data provided by the HCP database, which followed the HCP FIX-denoising pipeline (Glasser et al., 2013; Smith et al., 2013b). The processing mainly included correction for EPI distortion, temporal filtering (high-pass filter with 2,000 s), and nonaggressive regression of the structured artifacts identified by ICA-FIX (Griffanti et al., 2014; Salimi-Khorshidi et al., 2014) and 24 confound time series derived from the motion estimation (Satterthwaite et al., 2013). The rfMRI data were finally represented in the standard grayordinate space (91,282 grayordinates: cortical surface vertices plus subcortical gray matter voxels) by using multimodal surface matching (Robinson et al., 2014, 2018).

To validate the cortical distribution of the two indexes (CoRS and CoRI), we also used data from the Lifespan Human Connectome Project in Development (HCP-D, Lifespan HCP Release 1.0; Somerville et al., 2018). Only the healthy adults (age \geq 18 years) who had 4×6.5 min runs of rfMRI data were included (111 subjects, ages 18-22 years, 62 females). The resting-state fMRI (rfMRI) data were acquired on a 3 T Siemens Prisma platform with a 32-channel head coil. Briefly, a gradient-echo EPI sequence (478 time frames; TR=800 ms; TE=37 ms; flip angle, 52° ; 2.0 mm isotropic voxels; multiband factor, 8) was adopted for scanning each run of rfMRI data collected with eyes open. More details about the rfMRI acquisition were available in the published description of the HCP-D database (Harms et al., 2018). The preprocessing pipeline followed the publicly available HCP pipeline v4.1.3 (more details https://github.com/Washington-University/Pipelines).

Behavior data. Capitalizing on the behavior measures (BMs) provided by the HCP database for each participant (the open-access ones), we included 59 BMs covering six categories including alertness, cognition, emotion, motor, sensory, and personality. More details are provided in ConnectomeDB (https://db.humanconnectome.org). We only included the unadjusted scale score when it was applicable. These assessments represented general domains of human behavior. For the analysis related to these BMs, we only considered participants with both 59 measures and four completed rfMRI runs, which restricted the samples to 974 participants (ages 22–37 years, 514 females).

Cortical myeloarchitecture data. Three measures of the cortical myeloarchitecture were included in this study. Specifically, we selected the T1w/T2w ratio (Glasser and Van Essen, 2011), neurite density index (NDI; Fukutomi et al., 2018), and orientation dispersion index (ODI; Fukutomi et al., 2018), which were estimated based on the HCP dataset. The group averages of these data are publicly available (for the T1w/T2w ratio, https://balsa.wustl.edu/wN6Zv; for the cortical NDI and ODI, https://balsa.wustl.edu/study/show/k77v).

Gene expression data and preprocessing. We adopted the regional microarray-based expression data of the Allen Human Brain Atlas (AHBA; Hawrylycz et al., 2012), which consisted of over three thousand spatially distinct samples of brain tissues from six neurotypical postmortem adult brains. Because two brains were sampled on both hemispheres

and the other four brains only had samples from the left hemispheres in the AHBA dataset, we only used the data mapped to the left hemisphere. The preprocessed AHBA gene expression data are now publicly available along with their published guidelines (Arnatkeviciute et al., 2019). We adopted the preprocessed data updated on 11 June 2020. The gene expression data were mapped to the HCP multimodal parcellation 1.0 atlas (HCP atlas; Glasser et al., 2016). Since 3 out of 180 regions of the HCP atlas were excluded because of the data quality control of the expression measures, the size of the final region \times gene matrix was $177 \times 15,745$.

Group independent component analysis. A group ICA was conducted to detect a set of spatially independent components (ICs) across the participants in HCP S1200 release. The group ICs were utilized to guide the derivation of the individualized spatial maps and time series. By tuning the number of ICs, low-/high-dimensional group ICs were found to capture large-scale RSNs or their corresponding subnetworks (Beckmann, 2012; Smith et al., 2013a, 2015; Glasser et al., 2016; Lv et al., 2018). Here, we used RSNs to generally describe the spatial ICs derived from ICA decompositions.

A set of sequential steps were used to conduct the group ICA for the large dataset. First, the rfMRI data from each run was spatially demeaned and then normalized to remove the unstructured noise (Glasser et al., 2016). After that, the four runs from each participant were temporally concatenated to form a full run with 4,800 time frames. Second, to carry out the group principal component analysis (PCA) for the large dataset at a feasible memory cost, we adopted MELODIC's Incremental Group-PCA (MIGP) algorithm (Smith et al., 2014). We kept the dimension of the MIGP at 4,500. Third, a Wishart RollOff was performed to normalize the unstructured noise in the PCA space. More information about this processing is available in the Supplementary Methods of Glasser et al. (2016). Finally, the group ICA was conducted using the processed PCA series (dimension = 4,500) by using FSL's MELODIC tool (Beckmann and Smith, 2004). The ICA was run using a wide range of numbers of ICs (dimension, 25-150 at intervals of 1 and 150-300 at intervals of 5). The purpose was to select several representative dimensionalities by following Glasser et al. (2016) approach (Glasser et al., 2016). In brief, the operation was designed to detect the dimensionality that could describe the data with the smallest number of spatial clusters for which the corresponding surface area (or volume size) exceeded 25 mm² (or 125 mm³). As suggested in Glasser et al.'s analyses (Glasser et al., 2016), we chose to select the last local minimum which would be the one before the number of subcortical and cerebellar clusters began to increase monotonically.

Individualized RSNs and the corresponding time series. Guided by the spatial ICs from the group ICA, the individualized RSNs and the corresponding time series were derived by following two sequential steps. The concatenated rfMRI data (4,800 time frames) for each participant, which had been spatially demeaned and normalized, were adopted here.

First, to compensate for the distortion and misalignment after spatial registration, we adopted a weighted regression (Glasser et al., 2016), which was adapted from the standard dual regression (Filippini et al., 2009) by incorporating the estimation of both the distortion and the misalignment from subject native space to standard space. The weighted regression was found to improve the detection of individualized RSNs (Glasser et al., 2016). The output from the weighted regression was individualized spatial maps of the RSNs. Second, to further refine the corresponding time series for each subject's RSN considering the bias caused by the assumption of spatial independence between the ICs (Bijsterbosch et al., 2019), we adopted the thresholded regression approach, which had better recovery of the ground truth temporal signals in simulations (Bijsterbosch et al., 2019). Specifically, the spatial maps from the weighted regression were applied using a threshold derived from a Gaussian/gamma mixture model (Beckmann et al., 2005; Bijsterbosch et al., 2019), which was fitted to a histogram of the grayordinate values of a spatial map as one Gaussian distribution for the background lowweight signal and two gamma distributions (positive and negative intense signals). If the probability, which measured the extent that the signal of a grayordinate was from the gamma distributions rather than from the Gaussian distribution, was <0.5, the grayordinate would be excluded from the spatial map by setting the corresponding value to 0. The thresholded spatial maps were then regressed against the subject rfMRI data to derive the refined time series of the RSNs.

Calculation of CoRS and CoRI. Generally, the calculation of vertexwise CoRS and CoRI was based on the expression of RSNs at each cortical vertex, which was measured by the partial correlation coefficient between the time series of the vertex and each RSN. The CoRS and CoRI were defined to measure the extent of specific and average expression of RSNs at each vertex. In detail, we first derived the expression of RSNs at each brain location for each participant. Let $ts_{i,j}$ be the time series (1 × 4,800) of the *i*th grayordinate of participant j and TS_i^k be the time series $(1 \times 4,800)$ of the kth RSN of participant j, derived from the thresholded regression. To control the effects from other signal sources, we then employed a partial temporal correlation to measure the expression of the kth RSN at the ith grayordinate, that is, pcorr(ts_{ij}, TS_j^k | TS_j¹, ..., TS_j^{k-1}, TS_j^{k+1}, ..., TS_j^N) where pcorr is the partial temporal correlation and N is the number of RSNs. To achieve a stable estimate of the partial correlation coefficients, we used the ridge regression in FSLNets (L2-norm regularization, regularization parameter rho = 0.1; http://fsl.fmrib.ox.ac.uk/fsl/fslwiki/FSLNets). The derived spatial map (S_i^k) corresponded to the spatial expression of the kth RSN in the jth participant.

Second, with respect to each S_j^k , we adopted the Gaussian/gamma mixture model (Beckmann et al., 2005) to contrast the difference between the background random-like weights and the intensely positive or negative signals that were associated with a specific RSN. Because one Gaussian distribution and two gamma distributions were used to fit the histogram of S_j^k , the Gaussian probability density function (PDF) for the kth RSN of the jth participants is set as pdf $_{\text{Gaussian}}^{k,j}$. Correspondingly, the PDF of the gamma distribution for the positive signals is pdf $_{\text{Gammal}}^{k,j}$, and the one for the negative signals is pdf $_{\text{Gammal}}^{k,j}$, and the one for the negative signals is pdf $_{\text{Gammal}}^{k,j}$ and the interpolation of (Beckmann and Smith, 2004) to fit the mixture model. We then obtained the parameters of the PDFs and their corresponding weights. Specifically, $\lambda_0^{k,j}$ is the weight for pdf $_{\text{Gaussian}}^{k,j}$, $\lambda_1^{k,j}$ for pdf $_{\text{Gammal}}^{k,j}$, and $\lambda_2^{k,j}$ for pdf $_{\text{Gammal}}^{k,j}$. Using the fitted PDFs and weights, we defined the expression of the kth RSN at the ith grayordinate for the ith participants as follows:

$$p_{i,j}^k = \operatorname{prob}_{i,j}^k * \operatorname{PGamma}_{i,j}^k$$
,

where prob $_{i,j}^k$ is the probability that the value of the ith grayordinate was from the gamma distributions and PGamma $_{i,j}^k$ is the cumulative probability of the ith grayordinate based on the pdf $_{\mathrm{Gamma1}}^{kj}$ or pdf $_{\mathrm{Gamma2}}^{kj}$, which was decided by the sign of the corresponding value. The prob $_{i,j}^k$ is defined as follows:

$$\text{prob}_{ij}^k \ = \ \frac{\lambda_1^{kj} * \text{pdf}_{\text{Gammal}}^{kj}(\nu_{ij}^k)}{\lambda_0^{kj} * \text{pdf}_{\text{Gaussian}}^{kj}(\nu_{i,j}^k) + \lambda_1^{kj} * \text{pdf}_{\text{Gammal}}^{k,j}(\nu_{i,j}^k)}, \ \nu_{i,j}^k > 0,$$

$$\text{prob}_{i,j}^k \ = \ \frac{\lambda_2^{k,j} * \operatorname{pdf}_{\operatorname{Gamma2}}^{k,j}(v_{i,j}^k)}{\lambda_0^{k,j} * \operatorname{pdf}_{\operatorname{Gaussian}}^{k,j}(v_{i,j}^k) + \lambda_2^{k,j} * \operatorname{pdf}_{\operatorname{Gamma2}}^{k,j}(v_{i,j}^k)}, \ v_{i,j}^k < 0,$$

here, the $v_{i,j}^k$ is the partial correlation coefficient between the time series of the ith grayordinate and the kth RSN in the jth participant. The prob $_{i,j}^k$ was used to measure the normalized ratio between the signal and background noise. The PGamma $_{i,j}^k$ evaluated the signal strength within the distribution of signals.

Finally, we described the definition of the CoRS and the CoRI using $p_{i,i}^k$. In detail, the CoRS is defined as follows:

$$CoRS_{i,j} = \frac{\sqrt{N\left(\sum_{k=1}^{N} (p_{i,j}^{k} - E(p_{i,j}^{k}))^{2}\right)}}{\sqrt{(N-1)\sum_{k=1}^{N} p_{i,j}^{k}}}.$$
 (1)

Also, the CoRI is defined as follows:

$$CoRI_{i,j} = mean(p_{i,j}^k)$$
 (2)

where $CoRS_{i,j} \in [0, 1]$ and $CoRI_{i,j} \in [0, 1]$. Based on the definition, CoRS could quantify the extent that the RSNs specifically expressed at a grayordinate. When only one RSN had a nonzero expression value at a grayordinate, that is, only one RSN specifically expressed here, CoRS would be one. When a grayordinate had the same expression value for all RSNs, that is, RSNs evenly expressed here, CoRS at this grayordinate would be zero. CoRI represented the intensity of the expressions of RSNs. The larger the value, the stronger the intensity. Additionally, for the analysis using CoRS and CoRI, we focused on the cortical surface. A surface-based smoothing (sigma = 2 mm for the Gaussian kernel) was applied to the individual cortical maps of CoRS and CoRI by using the connectome workbench (Marcus et al., 2011) before running further analyses.

For the validate data in the HCP-D dataset, we ran the same analytic steps as described above, except that we set the dimension as 1,800 (1,912 time frames for the concatenated rfMRI data) for running the MIGP analysis, as the comparatively short scanning time. In addition, we did not run another optimal dimension search for the group ICA. Instead, we directly used the previously determined one (131) by considering the large sample size of the main analysis.

Hierarchical CoRS and CoRI. To further demonstrate whether CoRS and CoRI could reflect the neural basis of network coordination across the hierarchy of brain network organization, we proposed a hierarchical version of the two indexes based on the hierarchical clustering results derived by using the inter-RSNs temporal correlation (the similarity matrix across RSNs; Smith et al., 2015). In detail, for each participant, we calculated Pearson's correlation between the time series of any two RSNs from the thresholded regression to derive the individual network matrix. The corresponding correlation coefficients were converted into z statistics using Fisher's transformation. We then averaged the individual z-statistic matrices to deduce the group-averaged network matrix. Next, Ward's hierarchical clustering was applied to the group-averaged network matrix using the FSLNets toolbox. We mainly focused on three hierarchical levels to detect the clusters, including 4, 7, and 17 clusters, which had been previously found (Yeo et al., 2011; Smith et al., 2015). For the *i*th grayordinate of subject *j*, the involvement with the *k*th RSN had been previously defined as $p_{i,j}^k$. After deriving the clustering results, each RSN was allocated to a specific cluster c. We then defined the involvement of the *i*th grayordinate with the *c*th cluster of subject $j(p_{i,i}^c)$ as the maximal $p_{i,j}^k$ within cluster c. That is, $p_{i,j}^c = \max(p_{i,j}^k)$, $k \in \text{cluster } c$. Finally, the hierarchical CoRS and CoRI were calculated by using Equations 1 and 2, except for replacing $p_{i,j}^k$ with $p_{i,j}^c$.

Modeling the association between behaviors and CoRS/CoRI. Following the canonical correlation analysis (CCA) in Smith et al. (2015), we included three steps to detect the multivariate brain-behavior association. First, a set of confounders were regressed out from the brain and behavior variables before running the CCA. These confounders were (1) the version of the reconstruction software for the HCP data (two versions, coded as 1 and 0), (2) the average head motion across four runs of rfMRI, (3) the total intracranial volume (TIV), and (4) age, age², sex, age × sex, and age² × sex. Before regressing the confounders, a rank-based inverse Gaussian transformation was applied to the behavior variables to guarantee Gaussianity (Smith et al., 2015). Second, given the high dimension of the brain variables, we employed PCA to reduce the dimension of the brain variables (dimension, 59; the same as the number of BMs; the proportion of variance explained, 44.7% for CoRS, 47.3% for CoRI) to avoid overfitting the CCA model. The significance of the association between the brain canonical variable and the behavior canonical variable was determined by using a permutation test based on the PALM tool (Winkler et al., 2014), considering the family relationships within the HCP data. After each permutation, the maximal canonical correlation between canonical variables was recorded. The significance was decided based on the distribution of these maximal coefficients to control the family-wise error (FWE) rate for multiple comparisons. Finally, by

using Pearson's correlations, the significant brain and behavior canonical variables were respectively related to the brain and behavior variables in which the confounders had been regressed out. That is, each behavior variable was correlated with the behavior canonical variable, and the vertex-wise brain variables were correlated with the brain canonical variable.

Transcriptomic and functional enrichment analyses. To identify the transcriptional profiles underpinning the cortical distribution of CoRS and CoRI, a Spearman correlation analysis between the region-wise (HCP atlas) group-average transcriptional data (each gene in the AHBA data) and the region-wise group-average CoRS/CoRI was conducted. To consider the effect of spatial autocorrelation on the significance of the correlation, we adopted BrainSMASH (Burt et al., 2020) to conduct a permutation test to determine the corresponding p value. Then, we used the Gene Ontology enRIchment analysis and visuaLizAtion tool (GORILLA; Eden et al., 2009) to determine the functional enrichments of a target gene list that was compared with the background full gene set (15,745 genes). To visualize the key gene ontology (GO) terms related to the target gene list, we adopted the REVIGO (Supek et al., 2011) to project them into a two-dimensional space based on the semantic similarity between them.

Results

Briefly, we overviewed the data and the analytic steps adopted to generate the following results. Firstly, by using the rfMRI data of 1,003 young adults from the Human Connectome Project (HCP; Van Essen et al., 2013), we identified the brain functional networks, that is, resting-state networks (RSNs), including their spatial layouts and temporal activities, for each individual guided by the combination of the group template optimized for the entire sample and the estimation of individual variability (see more details in Materials and Methods). We determined the number of RSNs as 131 corresponding to the last local minimum, after which the subcortical and cerebellar components started to monotonically increase with the local minimum. Secondly, based on the expression values of RSNs at each cortical vertex, we calculated the CoRS and CoRI to measure the extent of specific and average expression of RSNs, outlining the topological signatures of co-representation. Thirdly, we sought the neural basis underlying the quantified pattern of co-representation in the brain by considering the myelin-related neuroanatomical measures and transcriptional profiles. Finally, we evaluated the biological significance of manifesting the observed co-representation pattern in the brain by testing the brain-behavior covariation.

The topological signatures of co-representation are anchored along a sensory–fugal axis of cytoarchitectural classes and consistent across the hierarchical levels of functional network Leveraging the individualized functional networks derived above, we had the co-representation of networks at each vertex, from which we calculated the CoRS and CoRI to measure the brainwide topological signatures of co-representation for each individual.

In detail, the group-average cortical distribution of CoRS is shown in Figure 2A. That is, these regions showing high CoRS values were mainly found in the somatosensory and motor cortex, primary auditory cortex, primary visual cortex, and retrosplenial cortex. In parallel, these regions showing high CoRI values were mainly found in the inferior/superior parietal cortex, middle temporal gyrus, precuneus, and dorsolateral/dorsomedial prefrontal cortex in terms of the group-average cortical distribution of CoRI (Fig. 2B). By projecting the cortical vertices to a two-dimensional space spanned by the z scores of the group-average CoRS and CoRI, three kinds of apices were found to outline the

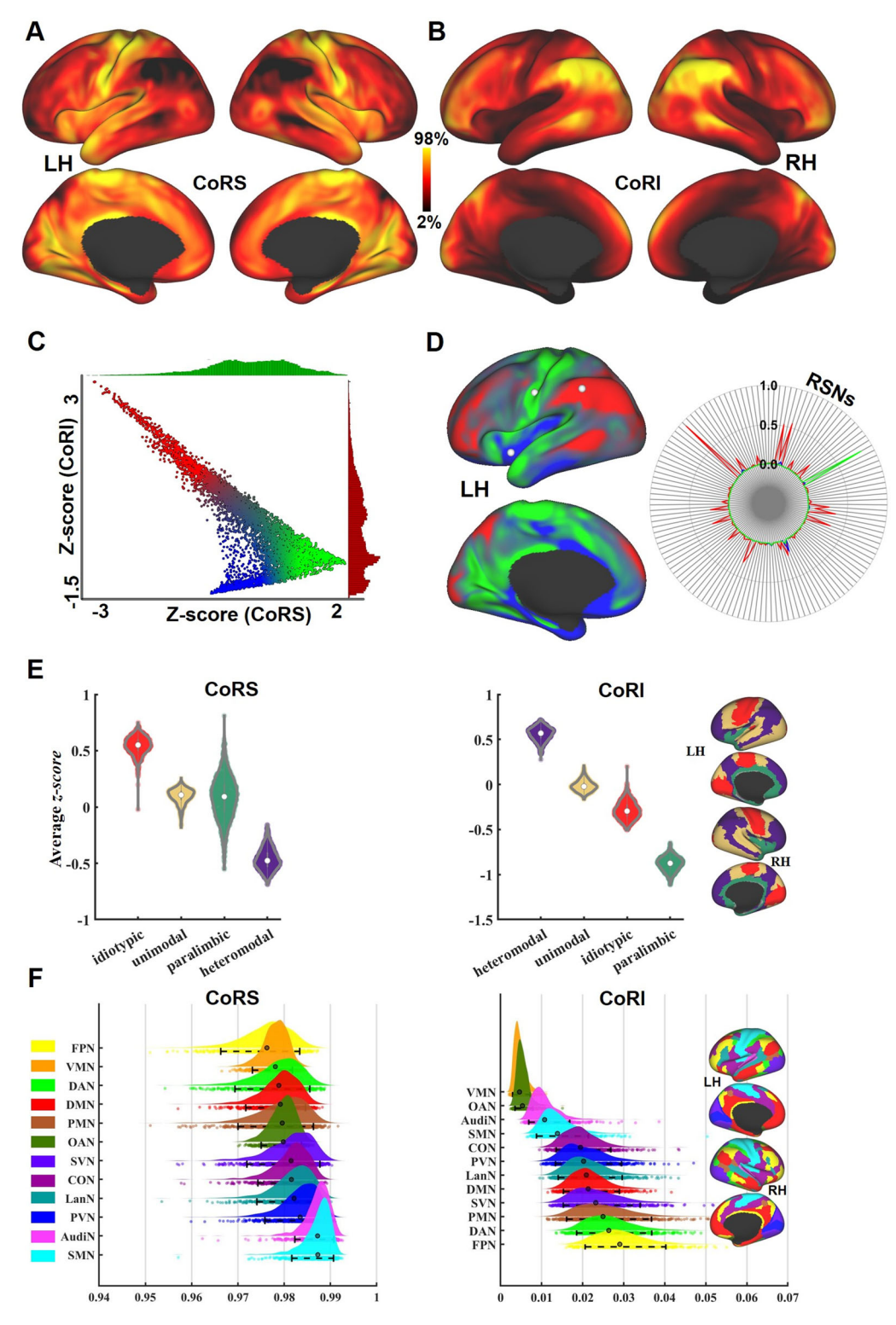


Figure 2. Cortical distributions of CoRS and CoRl. **A**, The group-average cortical map of CoRS. **B**, The group-average cortical map of CoRl. **C**, Scatterplot in the space spanned by the group-average CoRS and group-average CoRl. Each point represents a vertex. The z score of the group-average map is adopted for each axis. Histograms delineating the distribution of CoRS (green) and CoRl (red) are shown on the boundary. **D**, Left, Colors from the scatterplot are presented on the cortical surface. Three exemplary vertices are labeled as gray spheres. Right, A spider plot to show the co-representations of RSNs averaged across the subjects, respectively, for the three exemplary vertices. The colors correspond to their locations. **E**, The violin plot depicts the distribution of the within-area average of CoRS (left) and CoRl (right) in each individual. Before calculating the within-area average in each participant, the individual CoRS and CoRl maps were z scored. Each point within a violin plot represents a participant. Four colors shown on the brain surface indicate the cytoarchitectural classes (Mesulam, 2000; Paquola et al., 2019), that is, purple (heteromodal association areas), khaki (unimodal association areas), red (idiotypic areas), and green (paralimbic areas). **F**, The density plot depicts the distribution of the within-network mean of CoRS (left) and CoRl (right) in each individual. The networks (Ji et al., 2019) are visualized in different colors, abbreviated as ventral multimodal network (VMN), orbito-affective network (OAN), auditory network (AudiN), somatomotor network (SMN), language network (LAN), posterior multimodal network (PMN), secondary visual network (SVN), primary visual network (PVN), cingulo-opercular network (CON), dorsal attention network (DAN), default-mode network (DMN), and frontoparietal cognitive control network (FPN).

scope of the distribution, which were distinguished by different colors in Figure 2C. The three primary colors (red, green, and blue) corresponded to three kinds of extreme locations within the coordinate system spanned by CoRS and CoRI. The colors of the other vertices were coded according to their Euclidian distances to the three loci. These coded colors were further mapped back to the cortical surface to locate the corresponding brain regions (Fig. 2D, left column). To show an intuitive example of the distinct patterns of co-representation coded by the three primary colors, we randomly selected a vertex for each primary color (Fig. 2D, left column). The group-average pattern of co-representation of RSNs was distinct between each of the selected vertices (Fig. 2D, right column). A specific pattern of co-representation, that is, one RSN being preferentially expressed, was shown in the vertex selected from the green regions. In contrast, multiple RSNs were expressed in the vertex selected from the red regions. All RSNs showed low representation in the location picked from the blue regions. We also found the correspondence between and the brain space spanned by CoRS and CoRI and the cytoarchitectural classes along a sensory-fugal axis (Mesulam, 2000; Paquola et al., 2019). Specifically, the brain regions with green color (high CoRS) were mainly found in the idiotypic (primary) class, the brain regions with red color (low CoRS and high CoRI) were mainly found in the heteromodal class, and the brain regions with blue color (low CoRI) were mainly found in the paralimbic class (Fig. 2E). Significant differences in both CoRS and CoRI were found between the cytoarchitectural classes across the subjects (two-tailed $p < 1 \times 10^{-100}$; paired Wilcoxon signed rank test).

Moreover, we examined the distribution of both CoRS and CoRI across the predefined large-scale brain networks (Ji et al., 2019). By calculating the average value within each network of each individual, we showed the populational distribution of both CoRS and CoRI for each network (Fig. 2F). Regarding the populational average, the unimodal networks (Ito and Murray, 2022) including the somatomotor network (SMN), the auditory network (AudiN), and the primary visual network (PVN) were the top 3 based on their CoRS ranked in descending order, suggesting the specificity of the co-representation in the brain regions predefined in the unimodal networks. In contrast, the frontoparietal cognitive control network (FPN) presented the highest CoRI and the lowest CoRS, indicating that the brain regions predefined in the FPN were involved in multiple RSNs. We also confirmed the significance of pairwise difference between large-scale brain networks by using a paired Wilcoxon signed rank test between each pair of networks (two-tailed $p < 1 \times 10^{-5}$).

Furthermore, we used a hierarchical clustering approach to access other higher levels of the brain network organization. That is, we clustered the fine-grained RSNs (dimension, 131 as described above) into large-scale networks by taking the correlation between their time series as similarity measures. We tested three hierarchical levels of the clustering (4, 7, and 17 clusters). We found that the cortical distributions of both CoRS and CoRI showed high consistency across hierarchical levels (Fig. 3*A*,*B*). Pearson's correlation coefficient between group-

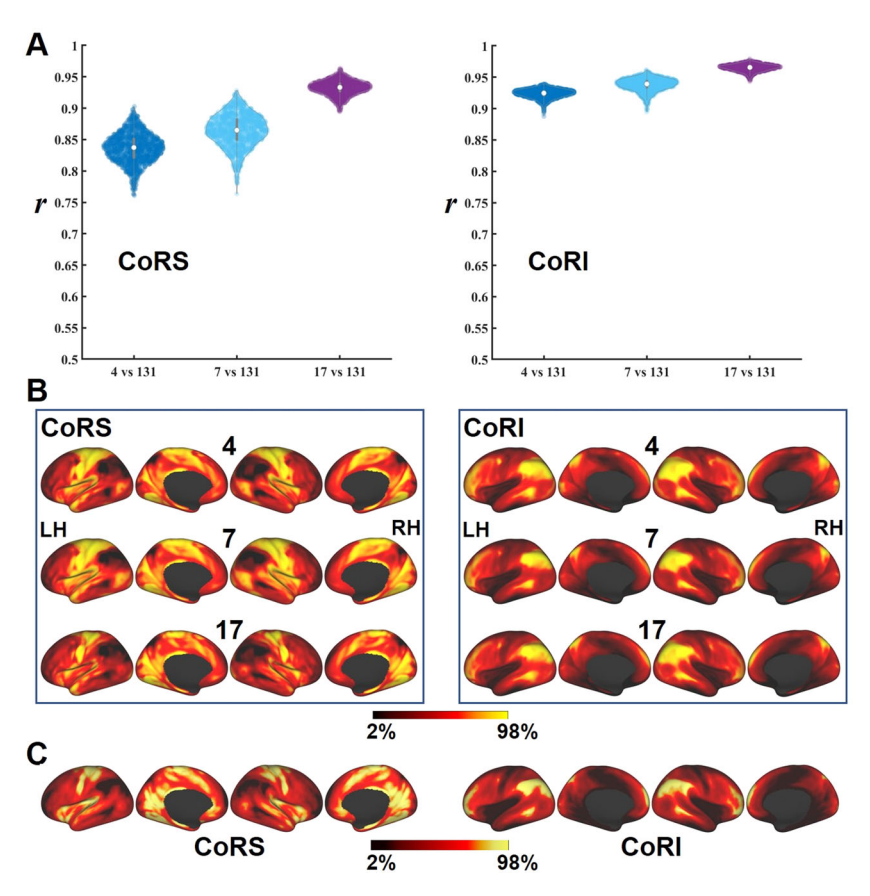


Figure 3. The distributions of CoRS and CoRI across the hierarchical levels of brain network organization and the validation in the external dataset. **A**, Each data point (blue, cyan, or purple) in the violin map represents Pearson's correlation coefficient for a participant between the different hierarchical levels (4, 7, and 17 networks, respectively) and the fine-grained level (131) regarding the CoRS map (left) and the CoRI map (right). The white circle represents the median value and the gray vertical bar represents the range from the first quartile to the third quartile. **B**, The group-average maps of CoRS (left) and CoRI (right) in different hierarchical levels. **C**, The group-average maps of CoRS (left) and CoRI (right) in the HCP-D dataset.

average cortical maps of CoRS was above 0.90, and the correlation between group-average cortical maps of CoRI was above 0.95. In addition, we tested the cortical distributions of both CoRS and CoRI in another independent dataset, that is, the adult data in the HCP-D dataset, by using the same computational approaches (see more details in the part of Materials and Methods above). With the same number of RSNs, that is, 131, we found that the group-average cortical map derived from the HCP-D dataset was highly similar to the current one (r = 0.95 for CoRI; r = 0.88 for CoRS; Fig. 3C).

The co-representation of brain networks is underpinned by the brain myeloarchitecture

To explore the biological underpinnings of the co-representation, we started with the brain myeloarchitecture by using the neuroanatomical measures and the transcriptional profiles, respectively.

First, we used three kinds of neuroanatomical measures to characterize the different aspects of cortical myelination, which included the myelin content measured by the ratio between the T1-weighted and T2-weighted MRI signals (Glasser and Van Essen, 2011), the cortical NDI, and the ODI. Both NDI and ODI were estimated from the neurite orientation dispersion and density imaging (NODDI) model (Zhang et al., 2012; Fukutomi et al., 2018). Specifically, we leveraged the groupaverage cortical maps of the three measures based on the HCP dataset in previous studies. By using Spearman correlation, we found a positive association between the group-average cortical maps of NDI and CoRS (r = 0.59; BrainSMASH-based p = 0.001; 1,000 permutations; Fig. 4A, left column) and a negative association between the group-average cortical maps of NDI and CoRI (r = -0.60; BrainSMASH-based p = 0.001; 1,000 permutations;Fig. 4A, right column). Here, the p values were determined by a permutation test using BrainSMASH (Burt et al., 2020), which generated 1,000 surrogate cortical maps that matched the spatial autocorrelation with the original group-average CoRS and CoRI maps. Moreover, similar associations were found between ODI and CoRS (r = 0.36; BrainSMASH-based p = 0.001), and between ODI and CoRI (r = -0.25; BrainSMASH-based p = 0.001). Finally, the cortical myelin content showed a positive association with the group-average cortical map of CoRS (r = 0.39; BrainSMASH-based p = 0.001). No significant association was found between the myelin content and the CoRI map (r = -0.04; BrainSMASH-based p > 0.15; 1,000 permutations).

Second, we employed the preprocessed region-wise transcriptional data (Arnatkeviciute et al., 2019) to establish the links between the gene expression and the cortical distributions of CoRS and CoRI. Specifically, by using Spearman correlation, the group-average transcriptional data that aligns to the brain regions in the left hemisphere of the HCP atlas was respectively linked to the group-average CoRS and CoRI. BrainSMASH was used to respectively generate 1,000,000 region-wise surrogate maps of CoRS and CoRI for the permutation tests. Based on the correlation coefficients, we ranked the included genes (15,745 genes) in descending order. The top 10% of the genes that also had statistical significance (BrainSMASH-based p < 0.05, uncorrected) were selected to conduct a GO enrichment analysis (591 and 1,209 genes for CoRS and CoRI, respectively). For CoRS, we found that the selected gene list was enriched for biological processes mainly including axon ensheathment, cell migration, regulation of cell growth, developmental process, and locomotion (p < 0.001; Fig. 4B, left column). For CoRI, the GO biological process enrichment included, for example,

potassium ion transport, response of glucose, and regulation of glucose metabolic process (p < 0.001; Fig. 4B, right column). In addition, given the associations of cortical myeloarchitectures with CoRS and CoRI, we tested the overlap between the selected gene list and the myelination gene set (Liu et al., 2019) by using the hypergeometric test (Hawrylycz et al., 2015). In detail, we found that the myelination gene set overlapped with the CoRS gene list (Fig. 4C, left; $p < 1.5 \times 10^{-9}$; 23 overlapped genes between 137 genes of the myelination gene set and 591 genes of the CoRS gene list), suggesting the over-representation of myelinationrelated genes in the CoRS gene list. To further test the specificity of the overlap between the CoRS-related gene set and the myelination gene set, we used several categorical gene sets including the brain-specific gene set, the synaptome gene set, and the oligodendrocyte gene set, which were provided in a recent paper (Burt et al., 2018). We confirmed that there was no significant overlap between the CoRS-related gene set and the brain-specific/synaptome gene set (p > 0.01) in the hypergeometric test). However, there was a significant overlap between the CoRS-related gene set and the oligodendrocyte gene set ($p < 1.2 \times 10^{-15}$; 133 overlapped genes between 1,769 genes in the myelination gene set and 591 genes in the CoRS-related gene set). Considering the important role of oligodendrocytes in myelination and axonal support (Simons and Nave, 2015), this result was consistent with the significant overlap between the CoRS-related gene set and the myelination gene set. Moreover, no significant overlap was found between the myelination and the CoRI gene sets (Fig. 4C, right; p > 0.48; 11 overlapped genes between 137 genes of the myelination gene set and 1,209 genes of the CoRI gene list).

The co-representation of brain networks covaries with individual behaviors

A further aim of this study was to understand the neurocognitive relevance of manifesting the co-representation. To accomplish this, we investigated the behavioral implications of the co-representation.

Specifically, we used the CCA to study the covariation between the pattern of co-representation (974 participants × 59,412 cortical vertices; CoRS or CoRI) and the corresponding behavioral performances (974 participants × 59 BMs). We included 59 BMs covering six categories including alertness, cognition, emotion, motor, sensory, and personality. By using CoRS as the brain variable, a pair of canonical variables were identified through CCA (r = 0.55; permutation-based p = 0.001; FWE corrected; 1,000 permutations; Fig. 5A). The correlation coefficient between the brain canonical variable and the CoRS values for each vertex across participants (vector size 974×1) was determined by Pearson's correlation (Fig. 5B). To further illustrate the difference in the brain regions highlighted by the positive and negative coefficients, we compared the average CoRS of each participant within the regions showing positive associations (p < 0.01, uncorrected) and the average CoRS regarding negative associations (p < 0.01, uncorrected) by conducting a paired Wilcoxon signed rank test. In detail, the regions showing positive associations mainly focused on the unimodal regions, while the regions showing negative associations were mainly found in the transmodal regions (Fig. 6A). The taxonomy of unimodal and transmodal regions was from previous studies (Ito et al., 2020a; Ito and Murray, 2022). We found that the average CoRS was higher in the regions showing positive associations with the brain canonical variable, compared with the average CoRI within the regions showing negative associations (two-tailed $p < 1 \times$ 10^{-100} ; z value >20; paired Wilcoxon signed rank test; Fig. 6A).

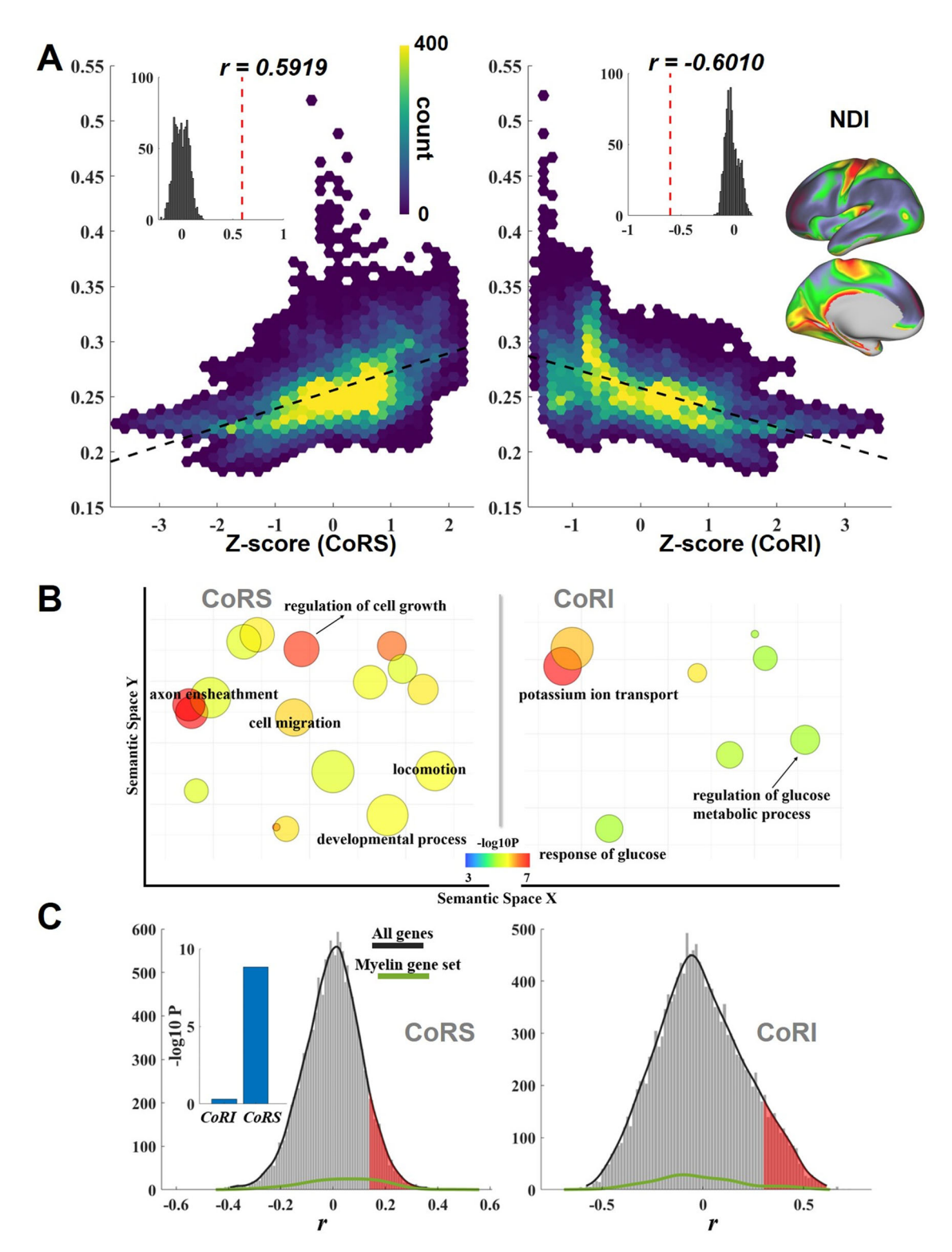


Figure 4. The cortical myeloarchitecture scaffolds the spatial distribution pattern of co-representation. $\textbf{\textit{A}}$, Association between the cortical NDI and the CoRS (left)/CoRI (right). The x axes correspond to the z scores of the two group-average indexes. The inset histogram shows the null distribution of the correlations derived from the BrainSMASH-based permutation. The red dashed line shows the original Spearman correlation coefficient. $\textbf{\textit{B}}$, Visualization of GO terms of biological processes in semantic space with respect to CoRS (left) and CoRI (right). The circle size indicates the frequency of the GO term in the database. $\textbf{\textit{C}}$, The density plots depict the distribution of Spearman correlation coefficients between CoRS (left) and CoRI (right) and transcriptional profiles. The black curve shows the estimated distribution of all genes included in the preprocessed AHBA data. The green curve represents the myelination gene set. The red-shaded area represents the top 10% of genes that also have significant associations with the index (BrainSMASH-based p < 0.05). The inset bar plot depicts the p values of the hypergeometric test which tested the overlap between the gene list of the red-shaded area and the myelination gene set.

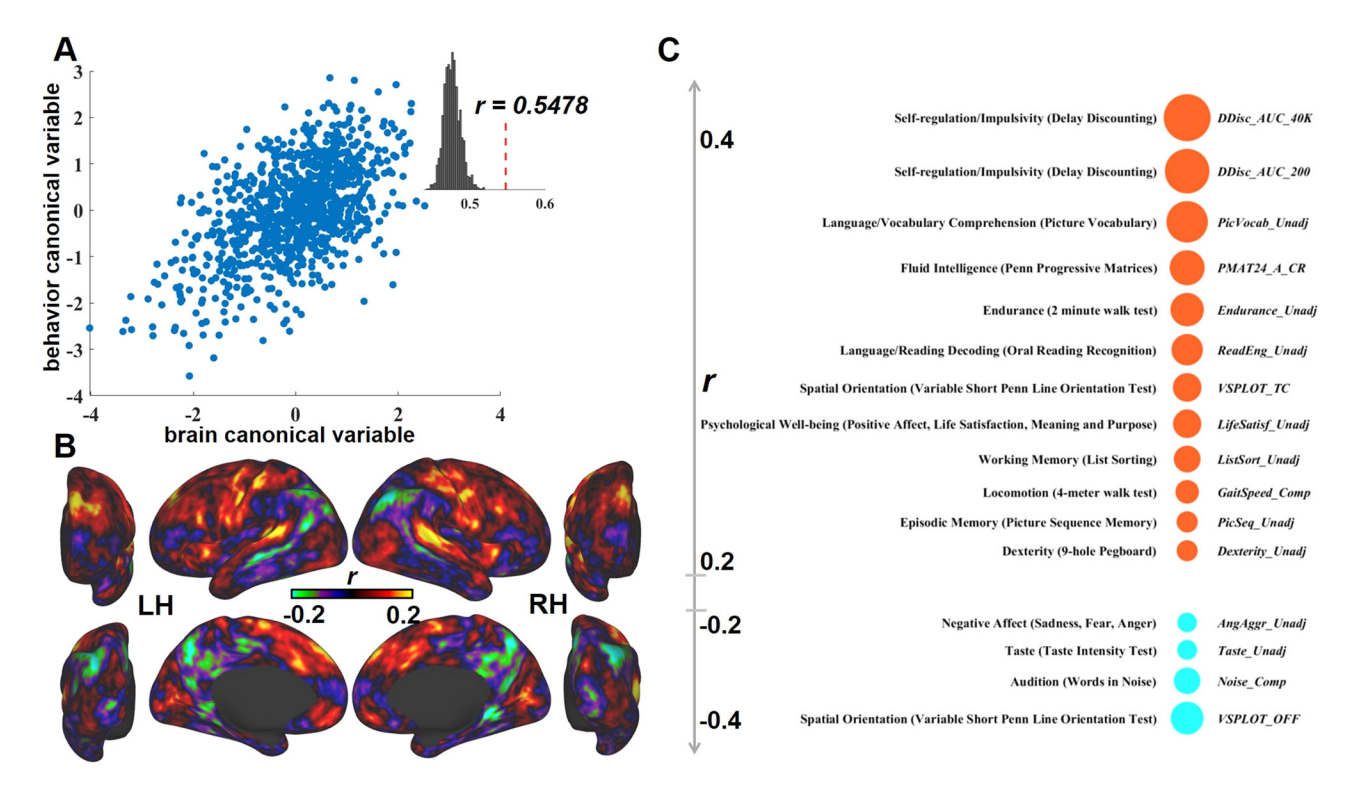


Figure 5. Covariation between CoRS and BMs. **A**, The significant covaried pattern between the behavior canonical variable and the brain canonical variable (canonical correlation r = 0.5478, pointed out by the red dashed line). Each blue point represents a participant. The inset histogram is composed of the maximal canonical correlation coefficient of each permutation (1,000 permutations). **B**, Cortical map of the vertex-wise correlation with the brain canonical variable. **C**, The BMs showing high correlations (r > 0.2) with the behavior canonical variable. The size of the circle corresponds to the absolute value of its Pearson's correlation coefficient. The coral circles represent the positive measures. The cyan circles represent the negative measures. A full description of each BM is available in ConnectomeDB (https://db.humanconnectome.org).

The difference still existed when using more conservative p values to define the corresponding regions (Fig. 6A). Similarly, the behavior canonical variable was linked to each BM by using Pearson's correlation. A BM was considered to be a positive (negative) measure if a high score acquired from the BM was indicative of a positive (negative) personal trait, a high (low) behavioral performance, or a high (low) quality of well-being. We found that BMs having positive correlation coefficients above 0.2 with the behavior canonical variable were positive measures, and BMs showing negative correlation coefficients below -0.2 were negative measures (Fig. 5C).

When using CoRI as the brain variable, there was also a pair of canonical variables that showed a significant correlation (r = 0.57; permutation-based p = 0.001; FWE corrected; 1,000 permutations). The correlation coefficient between the brain canonical variable and the CoRI values for each vertex across participants (vector size 974×1) was also determined by Pearson's correlation. The CoRI-based results were similar to the CoRS-based ones, in which a high correlation was found between the CoRI-based brain canonical variable and the CoRS-based one (r = 0.73) and between the CoRI-based behavior canonical variable and the CoRS-based one (r = 0.90). Further, we found that the average CoRI was higher within the regions showing positive associations with the CoRI-based brain canonical variable (twotailed $p < 1 \times 10^{-100}$; z value >20; paired Wilcoxon signed rank test; Fig. 6B), compared with the average CoRI within the regions showing negative associations. Similarly, most of the BMs that had positive correlation coefficients above 0.2 with the CoRI-based behavior canonical variable were positive measures, except for one BM which was for the median reaction time of correct responses in a fluid intelligence test. The BMs showing negative correlation coefficients below -0.2 were all negative measures.

Discussion

In this study, we leveraged the proposed approach of co-representation to disclose the neural basis underlying the well-observed phenomenon of spatial coordination among functional brain networks. The results of our multimodal analysis enabled new accounts of how the brain functional networks are spatially coordinated and what the coordination is for. Our study also provided a framework for extracting the system-wide coordination of brain networks for each individual, highlighting the potential in understanding individual brain patterns.

This work was built on the RSNs identified from the spontaneous BOLD signals in the human brain, which had proven effectiveness in characterizing the canonical brain functional networks (Smith et al., 2009; Gordon et al., 2017; Kong et al., 2019; Uddin et al., 2019; Bijsterbosch et al., 2020, 2021). Recent evidence suggests that RSNs reflect the baseline network state to support the cognitive task information transfer, constituting the intrinsic functional network architecture which is present regardless of external stimuli (Cole et al., 2014; Krienen et al., 2014; Ito et al., 2017; Gratton et al., 2018). Moreover, RSNs can directly predict brain responses to various cognitive stimuli (Tavor et al., 2016; Cohen et al., 2020), indicating their contribution to neurocognitive computations. Therefore, the co-representation of RSNs may depict an intrinsic latent space in which the brain can further fine-tune the configuration of the functional organization according to the external or internal contexts of stimuli. Our claim here is consistent with the perspective that describes the brain's functional organization as a

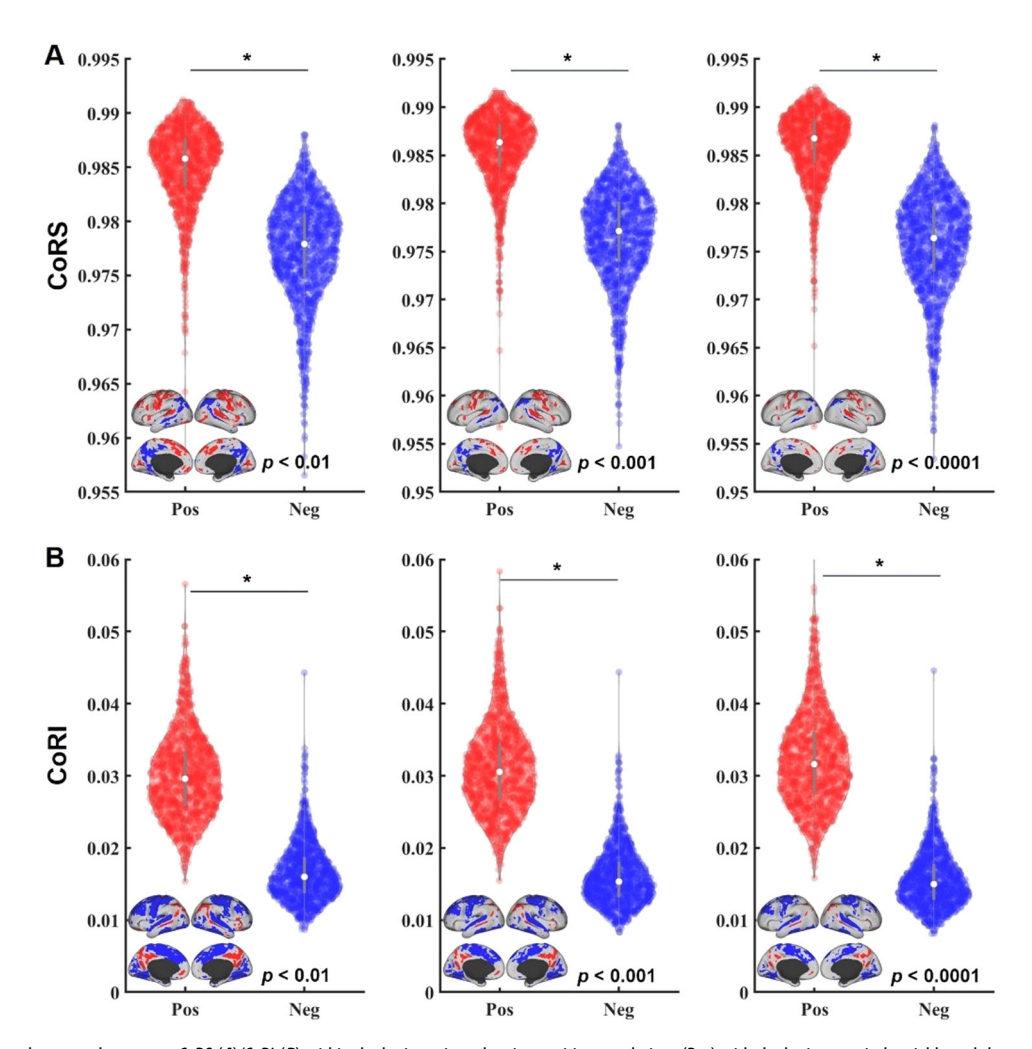


Figure 6. Comparison between the average CoRS (A)/CoRI (B) within the brain regions showing positive correlations (Pos) with the brain canonical variable and the average CoRS/CoRI within the brain regions showing negative correlations (Neg). Each data point (blue or red) in the violin map represents the average value within the corresponding brain regions below (blue or red) of each subject (974 subjects in total). The brain regions are defined according to the p values presented at the bottom right, which are used as thresholds to binarize the correlations with the brain canonical variable. The white circle in the violin map represents the median value, and the gray vertical bar represents the range from the first quartile to the third quartile. The paired Wilcoxon signed rank test was employed. * indicates a significant difference between Pos and Neg ($p < 1 \times 10^{-100}$; z > 20).

generative model which can generate and optimize top-down processes triggered by bottom-up stimuli or internal signals (Friston, 2005; Friston et al., 2017). Especially, the brain activity at rest is posited to maintain and optimize the brain's generative models for keeping options of future interactions open by preparing generic priors that can be characterized as the RSNs (Pezzulo et al., 2021). Supporting this, the quantified pattern of co-representation may facilitate our understanding of the spatial coding used by the brain for the model optimization at rest.

By looking into the co-representation patterns in the brain regions included by the predefined large-scale brain networks, we found that the frontoparietal network showed the highest CoRI averaged within the network and the unimodal networks including the SMN, the auditory network, and the PVN were the top 3 in the list of CoRS. This was reminiscent of the flexible hub theory that can explain the high variability in functional connectivity of the frontoparietal network both within itself and between other networks across a wide variety of tasks (Cole et al., 2013; Dixon et al., 2018; Cocuzza et al., 2020). The brain networks conjunctively represented within the spatial locations of the frontoparietal network may be the preconfigured neural basis supporting the flexible shift of connectivity pattern of the

frontoparietal network during the conduction of various cognitive tasks. In contrast, by showing a specific pattern of co-representation, the unimodal networks may respond to tasks more locally to ensure the input–output efficiency for information processing (Cole et al., 2013; Ito et al., 2020b). More interestingly, the brain regions showing high CoRI values were especially prevalent in regions maintaining the abstract representation of tasks during the generation of the learned rules (Vaidya et al., 2021). In short, these findings suggested that the spatial arrangement of the RSNs summarized by the co-representation might contribute to facilitating the functional flexibility that can be called for to abstract task representations for cognitive controls (Vaidya and Badre, 2022).

As the co-representation of RSNs is a functional representation of the brain network organization, we further dug into its biological underpinnings by integrating data from other modalities, which would help to delineate a more complete view of how the brain arranges the spatial layouts of the brain networks. Our results showed that higher CoRS (CoRI) was associated with higher (lower) cortical neurite density and neurite orientation dispersion, demonstrating that the cortical myeloarchitecture may play a crucial role in shaping the co-representation.

In particular, the cortical neurite density, reflecting the density of myelinated axons and not of myelin itself (Fukutomi et al., 2018), could explain the greatest variation in the spatial distribution of both CoRS and CoRI. This suggests that the density of myelinated axons may constrain how a cortical region is engaged in RSNs. The neurobiological effect of myelination adds two additional perspectives to increase the understanding of the above association. First, heavy myelination has been demonstrated to be related to rapid axonal conduction (Hartline and Colman, 2007), which is inversely correlated with intracortical circuit complexity (Glasser et al., 2014). Second, myelination has been found to inhibit both new axonal growth and synapse formation through molecular factors (Chen et al., 2000; McGee and Strittmatter, 2003), a finding which relates to intracortical circuit plasticity (Glasser et al., 2014). Therefore, myelination may shape the pattern of co-representation by affecting both the complexity and the plasticity of the intracortical circuit. Besides the underpinnings from the neuroanatomical factors of myeloarchitecture, our results also demonstrated the genetic influences on the co-representation by considering the cortical transcriptional profiles. Interestingly, the gene list of CoRS was found to be enriched for the axon ensheathment which is related to the process of neuronal myelination (Sherman and Brophy, 2005). This gene list was also over-represented in a predefined myelination gene set. These findings again confirmed the effect of myelination on shaping the co-representation, further indicating a pathway from microcosmic gene expressions to macrocosmic functional attributes via neuronal myelination processes.

Furthermore, our study was extended to understand the biological meanings for the brain to manifest the co-representation pattern. We demonstrated that the co-representations of RSNs could predict behavioral performance. By using the CCA, we identified highly similar patterns of brain-behavior covariation when using either CoRS or CoRI as the characterization of the co-representation. This could be accounted for by the fact that CoRS and CoRI delineate the two sides of the same principle of brain network organization. For the identified behavior canonical variable, it resembled a compositive behavioral measure on which highscoring subjects might have better performance in multiple domains of behaviors. Supporting this, we provided evidence that the behavior canonical variable showed a positive-negative correlation pattern corresponding with the positive and negative BMs. This pattern was consistent with the previous study (Smith et al., 2015), indicating that the identified behavior canonical variable tied to the co-representation of RSNs could comprehensively reflect the behavioral performance of subjects. When looking into the brain regions that strongly correlated with the brain canonical variable, a positive-negative correlation pattern emerged to separate the brain regions with the distinct pattern of the co-representation. If the co-representation was characterized by using CoRS, positive correlations were mainly found in brain regions with high CoRS and negative correlations were mainly found in brain regions with high CoRI. The same applied when using CoRI as the measure. These indicated that the brain regions with different patterns of co-representation played different roles in the prediction of behavioral performance, probably reflecting the functional separation between the unimodal cortex and the transmodal cortex in supporting human behaviors (Margulies and Smallwood, 2017). Considering the significant association between the behavior canonical variable and the brain canonical variable, these data suggested that the configuration of the co-representation of brain networks in the human brain has implications for the general performance of human behaviors.

In summary, by recapitulating the pattern of the co-representation of brain networks, our work here advanced our understanding of the orchestrated configuration of brain networks, especially its neural basis that existed in the brain myeloarchitecture and biological relevance found in brain functions and human behaviors. Our findings induce suggestions that may attract future work. First, it will be interesting to study the changes in the co-representation of brain networks, especially caused by psychiatric disorders, which may add new insights into the system-wide reconfiguration of brain networks. Second, given that localized ICA shows proven performance in specific brain regions (Leech et al., 2012; Braga et al., 2013; Igelstrom et al., 2015), it may be possible to extend the concepts of the co-representation of functional networks within specific brain areas. Finally, it will be desirable to further explore the genetic underpinnings of the co-representation in an enormous database, such as the UK Biobank (Miller et al., 2016; Bycroft et al., 2018), in which in-depth genetic and neuroimaging data are fully available.

References

Arnatkeviciute A, Fulcher BD, Fornito A (2019) A practical guide to linking brain-wide gene expression and neuroimaging data. Neuroimage 189: 353–367.

Bassett DS, Sporns O (2017) Network neuroscience. Nat Neurosci 20:353–364. Beckmann CF (2012) Modelling with independent components. Neuroimage 62:891–901.

Beckmann CF, DeLuca M, Devlin JT, Smith SM (2005) Investigations into resting-state connectivity using independent component analysis. Philos Trans R Soc Lond B Biol Sci 360:1001–1013.

Beckmann CF, Smith SM (2004) Probabilistic independent component analysis for functional magnetic resonance imaging. IEEE Trans Med Imaging 23:137–152.

Bijsterbosch JD, Beckmann CF, Woolrich MW, Smith SM, Harrison SJ (2019)
The relationship between spatial configuration and functional connectivity of brain regions revisited. Elife 8:e44890.

Bijsterbosch J, Harrison SJ, Jbabdi S, Woolrich M, Beckmann C, Smith S, Duff EP (2020) Challenges and future directions for representations of functional brain organization. Nat Neurosci 23:1484–1495.

Bijsterbosch JD, Valk SL, Wang D, Glasser MF (2021) Recent developments in representations of the connectome. Neuroimage 243:118533.

Braga RM, Sharp DJ, Leeson C, Wise RJ, Leech R (2013) Echoes of the brain within default mode, association, and heteromodal cortices. J Neurosci 33: 14031–14039

Burt JB, Demirtas M, Eckner WJ, Navejar NM, Ji JL, Martin WJ, Bernacchia A, Anticevic A, Murray JD (2018) Hierarchy of transcriptomic specialization across human cortex captured by structural neuroimaging topography. Nat Neurosci 21:1251–1259.

Burt JB, Helmer M, Shinn M, Anticevic A, Murray JD (2020) Generative modeling of brain maps with spatial autocorrelation. Neuroimage 220: 117038.

Bycroft C, et al. (2018) The UK Biobank resource with deep phenotyping and genomic data. Nature 562:203–209.

Chen J, et al. (2022) Shared and unique brain network features predict cognitive, personality, and mental health scores in the ABCD study. Nat Commun 13:2217.

Chen MS, Huber AB, van der Haar ME, Frank M, Schnell L, Spillmann AA, Christ F, Schwab ME (2000) Nogo-A is a myelin-associated neurite outgrowth inhibitor and an antigen for monoclonal antibody IN-1. Nature 403:434–439.

Cocuzza CV, Ito T, Schultz D, Bassett DS, Cole MW (2020) Flexible coordinator and switcher hubs for adaptive task control. J Neurosci 40: 6949–6968

Cohen AD, Chen Z, Parker Jones O, Niu C, Wang Y (2020) Regression-based machine-learning approaches to predict task activation using resting-state fMRI. Hum Brain Mapp 41:815–826.

- Cole MW, Bassett DS, Power JD, Braver TS, Petersen SE (2014) Intrinsic and task-evoked network architectures of the human brain. Neuron 83:238–251.
- Cole MW, Reynolds JR, Power JD, Repovs G, Anticevic A, Braver TS (2013) Multi-task connectivity reveals flexible hubs for adaptive task control. Nat Neurosci 16:1348–1355.
- Cui Z, et al. (2020) Individual variation in functional topography of association networks in youth. Neuron 106:340–353.e8.
- Cui Z, et al. (2022) Linking individual differences in personalized functional network topography to psychopathology in youth. Biol Psychiatry 92: 973–983
- Dadi K, Rahim M, Abraham A, Chyzhyk D, Milham M, Thirion B, Varoquaux G, Alzheimer's Disease Neuroimaging I (2019) Benchmarking functional connectome-based predictive models for resting-state fMRI. Neuroimage 192:115–134.
- Dixon ML, De La Vega A, Mills C, Andrews-Hanna J, Spreng RN, Cole MW, Christoff K (2018) Heterogeneity within the frontoparietal control network and its relationship to the default and dorsal attention networks. Proc Natl Acad Sci U S A 115:E1598–E1607.
- Eden E, Navon R, Steinfeld I, Lipson D, Yakhini Z (2009) GOrilla: a tool for discovery and visualization of enriched GO terms in ranked gene lists. BMC Bioinform 10:48.
- Filippini N, MacIntosh BJ, Hough MG, Goodwin GM, Frisoni GB, Smith SM, Matthews PM, Beckmann CF, Mackay CE (2009) Distinct patterns of brain activity in young carriers of the APOE-epsilon4 allele. Proc Natl Acad Sci U S A 106:7209–7214.
- Friston K (2005) A theory of cortical responses. Philos Trans R Soc Lond B Biol Sci 360:815–836.
- Friston KJ, Lin M, Frith CD, Pezzulo G, Hobson JA, Ondobaka S (2017) Active inference, curiosity and insight. Neural Comput 29:2633–2683.
- Fukutomi H, Glasser MF, Zhang H, Autio JA, Coalson TS, Okada T, Togashi K, Van Essen DC, Hayashi T (2018) Neurite imaging reveals microstructural variations in human cerebral cortical gray matter. Neuroimage 182:488–499.
- Genon S, Reid A, Langner R, Amunts K, Eickhoff SB (2018) How to characterize the function of a brain region. Trends Cogn Sci 22:350–364.
- Glasser MF, et al. (2013) The minimal preprocessing pipelines for the Human Connectome Project. Neuroimage 80:105–124.
- Glasser MF, et al. (2016) A multi-modal parcellation of human cerebral cortex. Nature 536:171–178.
- Glasser MF, Goyal MS, Preuss TM, Raichle ME, Van Essen DC (2014) Trends and properties of human cerebral cortex: correlations with cortical myelin content. Neuroimage 93:165–175.
- Glasser MF, Van Essen DC (2011) Mapping human cortical areas in vivo based on myelin content as revealed by T1- and T2-weighted MRI. J Neurosci 31:11597–11616.
- Gordon EM, et al. (2017) Precision functional mapping of individual human brains. Neuron 95:791–807.e7.
- Gratton C, et al. (2018) Functional brain networks are dominated by stable group and individual factors, not cognitive or daily variation. Neuron 98:439–452.e5.
- Griffanti L, et al. (2014) ICA-based artefact removal and accelerated fMRI acquisition for improved resting state network imaging. Neuroimage 95:232–247.
- Harms MP, et al. (2018) Extending the Human Connectome Project across ages: imaging protocols for the lifespan development and aging projects. Neuroimage 183:972–984.
- Hartline DK, Colman DR (2007) Rapid conduction and the evolution of giant axons and myelinated fibers. Curr Biol 17:R29–35.
- Hawrylycz MJ, et al. (2012) An anatomically comprehensive atlas of the adult human brain transcriptome. Nature 489:391–399.
- Hawrylycz M, et al. (2015) Canonical genetic signatures of the adult human brain. Nat Neurosci 18:1832–1844.
- Igelstrom KM, Webb TW, Graziano MS (2015) Neural processes in the human temporoparietal cortex separated by localized independent component analysis. J Neurosci 35:9432–9445.
- Ito T, Hearne LJ, Cole MW (2020a) A cortical hierarchy of localized and distributed processes revealed via dissociation of task activations, connectivity changes, and intrinsic timescales. Neuroimage 221:117141.
- Ito T, Hearne L, Mill R, Cocuzza C, Cole MW (2020b) Discovering the computational relevance of brain network organization. Trends Cogn Sci 24: 25–38
- Ito T, Kulkarni KR, Schultz DH, Mill RD, Chen RH, Solomyak LI, Cole MW (2017) Cognitive task information is transferred between brain regions via resting-state network topology. Nat Commun 8:1027.

- Ito T, Murray JD (2022) Multitask representations in the human cortex transform along a sensory-to-motor hierarchy. Nat Neurosci 26:306–315.
- Ji JL, Spronk M, Kulkarni K, Repovs G, Anticevic A, Cole MW (2019) Mapping the human brain's cortical-subcortical functional network organization. Neuroimage 185:35–57.
- Kong R, et al. (2019) Spatial topography of individual-specific cortical networks predicts human cognition, personality, and emotion. Cereb Cortex 29:2533–2551.
- Krienen FM, Yeo BT, Buckner RL (2014) Reconfigurable task-dependent functional coupling modes cluster around a core functional architecture. Philos Trans R Soc Lond B Biol Sci 369:20130526.
- Leech R, Braga R, Sharp DJ (2012) Echoes of the brain within the posterior cingulate cortex. J Neurosci 32:215–222.
- Liu S, Li A, Zhu M, Li J, Liu B (2019) Genetic influences on cortical myelination in the human brain. Genes Brain Behav 18:e12537.
- Lv H, Wang Z, Tong E, Williams LM, Zaharchuk G, Zeineh M, Goldstein-Piekarski AN, Ball TM, Liao C (2018) Resting-state functional MRI: everything that nonexperts have always wanted to know. Am J Neuroradiol 39:1390–1399.
- Marcus DS, Harwell J, Olsen T, Hodge M, Glasser MF, Prior F, Jenkinson M, Laumann T, Curtiss SW, Van Essen DC (2011) Informatics and data mining tools and strategies for the Human Connectome Project. Front Neuroinform 5:4.
- Margulies DS, Smallwood J (2017) Converging evidence for the role of transmodal cortex in cognition. Proc Natl Acad Sci U S A 114:12641–12643.
- McGee AW, Strittmatter SM (2003) The Nogo-66 receptor: focusing myelin inhibition of axon regeneration. Trends Neurosci 26:193–198.
- Menon V (2011) Large-scale brain networks and psychopathology: a unifying triple network model. Trends Cogn Sci 15:483–506.
- Mesulam MM (1990) Large-scale neurocognitive networks and distributed processing for attention, language, and memory. Ann Neurol 28:597–613.
- Mesulam MM (2000) *Principles of behavioral and cognitive neurology*, 2nd ed. Oxford, New York: Oxford University Press.
- Miller KL, et al. (2016) Multimodal population brain imaging in the UK Biobank prospective epidemiological study. Nat Neurosci 19:1523–1536.
- Paquola C, et al. (2019) Microstructural and functional gradients are increasingly dissociated in transmodal cortices. PLoS Biol 17:e3000284.
- Perovnik M, Rus T, Schindlbeck KA, Eidelberg D (2022) Functional brain networks in the evaluation of patients with neurodegenerative disorders. Nat Rev Neurol 19:73–90.
- Pezzulo G, Zorzi M, Corbetta M (2021) The secret life of predictive brains: what's spontaneous activity for? Trends Cogn Sci 25:730–743.
- Power JD, et al. (2011) Functional network organization of the human brain. Neuron 72:665–678.
- Robinson EC, et al. (2018) Multimodal surface matching with higher-order smoothness constraints. Neuroimage 167:453–465.
- Robinson EC, Jbabdi S, Glasser MF, Andersson J, Burgess GC, Harms MP, Smith SM, Van Essen DC, Jenkinson M (2014) MSM: a new flexible framework for multimodal surface matching. Neuroimage 100: 414–426.
- Rosenberg MD, Finn ES, Scheinost D, Papademetris X, Shen X, Constable RT, Chun MM (2016) A neuromarker of sustained attention from wholebrain functional connectivity. Nat Neurosci 19:165–171.
- Salimi-Khorshidi G, Douaud G, Beckmann CF, Glasser MF, Griffanti L, Smith SM (2014) Automatic denoising of functional MRI data: combining independent component analysis and hierarchical fusion of classifiers. Neuroimage 90:449–468.
- Salzer JL, Zalc B (2016) Myelination. Curr Biol 26:R971-R975.
- Satterthwaite TD, et al. (2013) An improved framework for confound regression and filtering for control of motion artifact in the preprocessing of resting-state functional connectivity data. Neuroimage 64:240–256.
- Sha Z, Wager TD, Mechelli A, He Y (2019) Common dysfunction of large-scale neurocognitive networks across psychiatric disorders. Biol Psychiatry 85:379–388.
- Sherman DL, Brophy PJ (2005) Mechanisms of axon ensheathment and myelin growth. Nat Rev Neurosci 6:683–690.
- Simons M, Nave KA (2015) Oligodendrocytes: myelination and axonal support. Cold Spring Harb Perspect Biol 8:a020479.
- Smith SM, et al. (2009) Correspondence of the brain's functional architecture during activation and rest. Proc Natl Acad Sci U S A 106:13040–13045.
- Smith SM, et al. (2013a) Functional connectomics from resting-state fMRI. Trends Cogn Sci 17:666–682.

- Smith SM, et al. (2013b) Resting-state fMRI in the Human Connectome Project. Neuroimage 80:144–168.
- Smith SM, Hyvarinen A, Varoquaux G, Miller KL, Beckmann CF (2014) Group-PCA for very large fMRI datasets. Neuroimage 101:738–749.
- Smith SM, Nichols TE, Vidaurre D, Winkler AM, Behrens TE, Glasser MF, Ugurbil K, Barch DM, Van Essen DC, Miller KL (2015) A positive-negative mode of population covariation links brain connectivity, demographics and behavior. Nat Neurosci 18:1565–1567.
- Somerville LH, et al. (2018) The Lifespan Human Connectome Project in Development: a large-scale study of brain connectivity development in 5-21 year olds. Neuroimage 183:456–468.
- Suarez LE, Markello RD, Betzel RF, Misic B (2020) Linking structure and function in macroscale brain networks. Trends Cogn Sci 24:302–315.
- Sui J, Jiang R, Bustillo J, Calhoun V (2020) Neuroimaging-based individualized prediction of cognition and behavior for mental disorders and health: methods and promises. Biol Psychiatry 88:818–828.
- Supek F, Bosnjak M, Skunca N, Smuc T (2011) REVIGO summarizes and visualizes long lists of gene ontology terms. PLoS One 6:e21800.
- Tavor I, Parker Jones O, Mars RB, Smith SM, Behrens TE, Jbabdi S (2016) Task-free MRI predicts individual differences in brain activity during task performance. Science 352:216–220.
- Uddin LQ, Yeo BTT, Spreng RN (2019) Towards a universal taxonomy of macro-scale functional human brain networks. Brain Topogr 32:926–942.
- Ugurbil K, et al. (2013) Pushing spatial and temporal resolution for functional and diffusion MRI in the Human Connectome Project. Neuroimage 80: 80–104
- Vaidya AR, Badre D (2022) Abstract task representations for inference and control. Trends Cogn Sci 26:484–498.

- Vaidya AR, Jones HM, Castillo J, Badre D (2021) Neural representation of abstract task structure during generalization. Elife 10:e63226.
- Van Essen DC, Smith SM, Barch DM, Behrens TE, Yacoub E, Ugurbil K, WU-Minn HCP Consortium (2013) The WU-Minn Human Connectome Project: an overview. Neuroimage 80:62–79.
- Winkler AM, Ridgway GR, Webster MA, Smith SM, Nichols TE (2014) Permutation inference for the general linear model. Neuroimage 92: 381–397.
- Wu EXW, Liaw GJ, Goh RZ, Chia TTY, Chee AMJ, Obana T, Rosenberg MD, Yeo BTT, Asplund CL (2020) Overlapping attentional networks yield divergent behavioral predictions across tasks: neuromarkers for diffuse and focused attention? Neuroimage 209:116535.
- Yamashita M, et al. (2018) A prediction model of working memory across health and psychiatric disease using whole-brain functional connectivity. Elife 7:e38844.
- Yang Z, et al. (2016) Genetic and environmental contributions to functional connectivity architecture of the human brain. Cereb Cortex 26:2341–2352.
- Yeo BT, et al. (2011) The organization of the human cerebral cortex estimated by intrinsic functional connectivity. J Neurophysiol 106:1125–1165.
- Zachlod D, Bludau S, Cichon S, Palomero-Gallagher N, Amunts K (2022) Combined analysis of cytoarchitectonic, molecular and transcriptomic patterns reveal differences in brain organization across human functional brain systems. Neuroimage 257:119286.
- Zhang H, Schneider T, Wheeler-Kingshott CA, Alexander DC (2012) NODDI: practical in vivo neurite orientation dispersion and density imaging of the human brain. Neuroimage 61:1000–1016.
- Zhao B, et al. (2022) Common variants contribute to intrinsic human brain functional networks. Nat Genet 54:508–517.